Ore Geology Reviews 114 (2019) 103131

Contents lists available at ScienceDirect

Ore Geology Reviews

journal homepage: www.elsevier.com/locate/oregeorev

Distribution of and hydrographic controls on ferromanganese crusts: Tropic Seamount, Atlantic

I.A. Yeo[a,b,*], S.A. Howarth[c], J. Spearman[d], A. Cooper[d], N. Crossouard[d], J. Taylor[d], M. Turnbull[d], B.J. Murton[a]

[a] National Oceanography Centre Southampton, European Way, Southampton SO14 3ZH, UK
[b] Kingston University, Penrhyn Road, Kingston-upon-Thames, Surrey KT1 2EE, UK
[c] University of Southampton, National Oceanography Centre, European Way, Southampton SO14 3ZH, UK
[d] HR Wallingford, Howbery Business Park, Crowmarsh Gifford, Wallingford OX10 8BA, UK

ARTICLE INFO

Keywords:
Ferromanganese crusts
Ferromanganese nodules
Seafloor mapping
Critical elements
Tropic Seamount
Atlantic

ABSTRACT

Hydrogenetic ferromanganese crusts are likely to be exploited as resources for critical metals in the near future, yet the processes controlling where and how they grow are poorly understood. Using detailed mapping of seafloor outcrop and well constrained hydrographic modelling alongside scanning electron microscope imagery of samples from the Tropic Seamount, a star-shaped guyot located in the Tropical East Atlantic, we investigate the relationship between currents, ferromanganese crustal texture and the locations and intensity of crustal erosion. Here, we report the distribution of FeMn crusts and explore factors controlling their growth and erosion. We find that just over 35% of the summit plateau of the guyot exposes some form of ferromanganese crust mineralisation, with the rest variably covered by plains of mobile sediment and slim cliff exposures of carbonate. The steep flanks of the guyot largely expose ferromanganese crust both *in situ* and as debris flows. The strongest currents are located on the upper flanks of the guyot, the central part of its eastern limb, and across the summit plateau. Three categories of surface morphologies are identified; from pristine botryoidal surfaces to flat areas that have been completely polished by the erosive action of currents and sediment. The relationship between the outcrop of crusts, their erosional states and the hydrographic current regime to which they are exposed is complicated. There is a general correlation between the degree of erosion and location across the seamount, with the least eroded being found on the flanks below 2000 m water depth and the most heavily eroded crusts largely restricted to the summit area. Furthermore, the pristine samples all reside in areas that rarely experience current magnitudes over 0.2 m/s, suggesting that above this the currents have the ability to erode ferromanganese crust. However, there is a strong overlap between the measured current magnitudes at the locations of partially and completely eroded crusts, as well as partial overlap with the current magnitudes measured at pristine crust locations. This complexity is likely due to the presence of cliffs and plateaus increasing current magnitudes and turbidity at a scale smaller than the model resolution.

1. Introduction

Marine hydrogenetic ferromanganese (FeMn) crusts are found throughout the Earth's oceans precipitating onto hard, indurated surfaces at water depths between 400 m and 7000 m (Hein and Koschinsky, 2014). FeMn crusts are a type of layered, metal rich mineralisation, containing high concentrations of Co, Ti, Mn, Ni, Pt, Zr, Nb, Te, Bi, Mo, W, Th and rare earth elements (REEs) (Hein et al., 2013; Hein and Koschinsky, 2014). A number of these have been defined as "critical elements", where predicted future demand, primarily due to increased global uptake of low-carbon ('green') technologies, is likely to outstrip supply (European Commission, 2017; Price, 2011). As a result there is increased interest in the exploitation of seafloor FeMn crusts as metal resources (Manheim, 1986; Hein et al., 2000; Clark et al., 1984; Hein et al., 2013; Rona, 2003; Hein et al., 2010; Lusty et al., 2018).

Although FeMn crusts are not currently being exploited as economic resources, several exploration contracts have been issued by the United Nations International Seabed Authority (ISA): five in the Pacific Ocean and one in the Atlantic ocean, on the Rio Grande Rise (Petersen et al., 2016). As Pacific crusts tend to be better studied than those in other oceans, primarily due to their likely greater thickness and hence economic potential, the majority of resource studies are based on these

* Corresponding author at: National Oceanography Centre Southampton, European Way, Southampton SO14 3ZH, UK.
E-mail address: i.yeo@noc.ac.uk (I.A. Yeo).

https://doi.org/10.1016/j.oregeorev.2019.103131
Received 14 June 2019; Received in revised form 27 August 2019; Accepted 16 September 2019
Available online 27 September 2019

samples (Hein et al., 2009). However, as the chemical differences between Pacific and Atlantic crusts are fairly minor (e.g. Koschinsky et al., 1995a,b), similar constraints would likely apply to possible Atlantic mining operations. Currently, sites at < 2500 m water depths, with average crustal thicknesses of > 3 cm, with little to no sediment cover, exposed across multiple 20 km^2 sub-blocks are considered to form realistic mining targets (Hein et al., 2009). Such a site would almost certainly need to extend across several different seamounts and its viability will be affected by the mining efficiency, which will vary with summit topography, crustal thickness and grade, as well as environmental protection requirements.

Crusts grow extremely slowly, typically on the order of a few mm per million years (Krishnaswami and Kirk Cochran, 1978; Ingram et al., 1990; Klemm et al., 2005; Banakar and Hein, 2000) and can range in thickness from a sub-millimeter thick coatings to more than 25 cm thick accretions (Hein et al., 2000). Crusts occur primarily on seamounts and ridges within the oceans, as they provide hard, rocky and commonly sediment free substrates onto which they can precipitate. Furthermore, they promote upwelling and mixing of deep oxygenated waters with the oxygen-minimum zone (OMZ), which is rich in dissolved Mn (Halbach and Puteanus, 1984). Rates of growth and crustal chemistry are thought to be controlled by the availability of Fe and Mn oxide colloids, with Mn coming from the breakdown of organic matter in the OMZ and Fe primarily from the dissolution of carbonate plankton (Halbach et al., 2017). These colloids are highly reactive, allowing them to scavenge a variety of dissolved cations and anions from the surrounding seawater (Koschinsky and Hein, 2003; Hein et al., 2000). Seamounts are abundant throughout the world's oceans (Wessel et al., 2010) and FeMn crusts are found globally with the oldest located in the northwest equatorial Pacific Ocean (Hein et al., 2000, 2009; Hein and Koschinsky, 2014). The internal structure of FeMn crusts is often complicated and commonly comprises a mixture of massive textures, laminated pillars and more chaotic cuspate/botryoidal regions, which contain higher percentages of detrital and bioclastic material (Banakar and Hein, 2000; Hein et al., 1992; Yeo et al., 2018). A single FeMn crust sample may show multiple different phases, alternating between growth and erosion (Banakar and Hein, 2000; Yeo et al., 2018).

Tropic Seamount (Fig. 1) is a guyot located in the tropical east Atlantic at the southernmost end of the Canary Seamount chain, forming part of the Western Saharan Seamount Province. This region has been continuously volcanically active since around 140 Ma, with the majority of activity occurring during the Miocene and minor activity continuing on El Hierro until around 0.2 Ma (van den Bogaard, 2013). Rising around 3000 m above the 155 Ma oceanic crust on which it sits (Josso et al., 2019), Tropic Seamount is characterised by a flat top and four distinct spurs formed by gravitation collapse of the flanks between them (Palomino et al., 2016; Vogt and Smoot, 1984; Mitchell, 2001). Volcanic rocks dredged from the seamount include basalts, trachybasalts and trachytes (Blum et al., 1996) erupted primarily between 119 and 114 Ma, with some minor volcanic activity possible until 60 Ma (van den Bogaard, 2013). The volcano is believed to have been subsiding and eroding since volcanic activity ceased and the summit now sits at a water depth of 950–1100 m. The flat-topped summit was produced by wave erosion during subsidence and is covered by the products of later reef growth and sedimentation. Tropic Seamount spans a variety of water masses: Antarctic bottom water bathes the flanks of the seamount below 3000 m, Classic Labrador Sea Water between 2000 and 3000 m water depth, and Upper Labrador Sea and Upper Circumpolar Deep Water between 1000 and 2000 m. These water masses, which form relatively planar layers, are typical of the water masses across this entire region and there is no evidence of high-energy dynamic mixing of water bodies in the vicinity of Tropic. The region is affected by the Canary Current, which supplies the area with cool, upwelled, nutrient-rich waters (Wooster et al., 1976; Mittelstaedt, 1991; Pelegrí and Peña-Izquierdo, 2015). Historical variability in the strength and nature of this current is documented from sediment studies (e.g. Sarnthein et al., 1982) and reflects global climatic events, with changes in temperature of up to 8 °C and movements and extensions of the current of up to 500 km. The area also receives periodic input of Saharan dust, which is correlated with lower FeMn crustal growth rates (Marino et al., 2017).

FeMn crusts have been retrieved and dated from Tropic Seamount by previous studies, including FeMn crusts of 4–10 cm thickness with ages up to 12 Ma and growth rates of 3.3–8.3 mm/Ma (Koschinsky et al., 1995a,b) and phosphatized samples with growth rates of 1.9–2.7 mm/Ma (Marino et al., 2017) and ages up to 30–40 Ma (Koschinsky et al., 1996). More recently FeMn crusts with ages up to 75 Ma have been located on the summit (Josso et al., 2019).

During expedition 142 on board the Royal Research Ship *James Cook* (hereafter referred to as JC142), FeMn crusts on Tropic Seamount were comprehensively surveyed and sampled (Yeo et al., 2018; Lusty et al., 2018, Josso et al., 2019). High-resolution geophysical surveys, visual observations of the seafloor and a large number of in-situ, accurately-located samples were collected in order to build up a comprehensive, detailed picture of the FeMn crustal resource present (Lusty and Murton, 2018), while moorings and CTD casts were used to develop a detailed hydrodynamic model. A variety of FeMn crust morphologies were observed (Lusty et al., 2018; Yeo et al., 2018), and dated (Josso et al., 2019). In this contribution, we present the results from detailed mapping of different lithologies from visual observations and geophysical datasets, alongside measured crustal thicknesses from samples and erosion states defined using a scanning electron microscope (SEM). By comparing these data to a well constrained hydrographic model, we can better assess the primary factors controlling crustal growth locations and thickness. Such advances have the potential to improve our ability to predict the locations of the best resources and distinguish areas that could be set aside for environmental protection.

2. Methods

2.1. Expedition JC142 to Tropic Seamount

All the data presented here were collected during expedition JC142 as part of the Marine E-tech project. During the expedition, a large array of equipment was used, including both the autonomous underwater vehicle (AUV) AUTOSUB 6000 and the remotely operated vehicle (ROV) Isis (both operated by the National Oceanography Centre Southampton). Details of the various datasets collected are summarised below.

2.2. Bathymetry and sidescan sonar

Bathymetry and backscatter data of the entire seamount was collected using the ship-mounted Kongsberg EM120 multibeam echosounder. Data were processed using Caris Hips and Sips and QPS Fledermaus and FM Geocoder Toolbox v7.6.3. Final grids and mosaics were produced at 50 m cell spacing. High-resolution bathymetry and backscatter were also collected using a Kongsberg EM2040 multibeam echosounder operating at 200 kHz and an Edgetech 4200 sidescan sonar operating at 100 kHz and 400 kHz mounted on the AUV. Bathymetric data were processed using MB-System (Caress, 1999) and navigation was adjusted using the feature mapping module "mbnavadjust" within MB-System then matched to ultra-short-baseline (USBL) positions measured from the ship to the AUV using the ship Sonardyne USBL at the start and end of missions. Sidescan sonar mosaics were produced using the QPS FM Geocoder Toolbox v7.6.3. Final bathymetric grids were produced at 2 m grid spacing and sidescan sonar mosaics at 0.5 m for both frequencies (due to the along track resolution controlled by the vehicle speed).

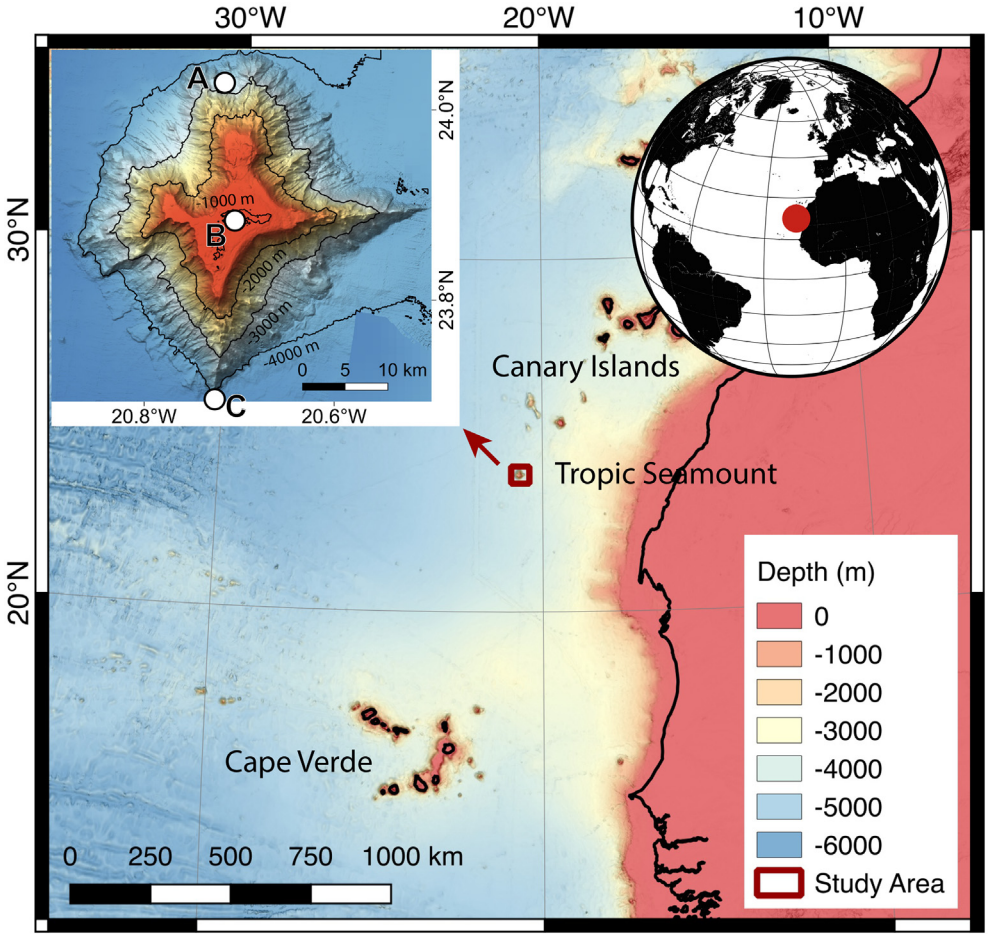

Fig. 1. Location of Tropic Seamount, which is a guyot rising from a 4000 m deep abyssal seafloor to a summit depth of 1100–900 m. Regional bathymetry is extracted from Sandwell et al. (2014) gridded at 30 s. Inset shows EM120 bathymetry collected during expedition JC142, and gridded at 100 m. Gaps have been filled using the Sandwell et al. (2014) grid. White dots A – C are mooring locations for current measurements.

2.3. Scanning electron microscope (SEM)

All the samples selected for analysis in this study were collected by the ROV manipulator arm. Samples were orientated using video footage of them on the seafloor recorded by the ROV. SEM imaging was carried out on the upper surfaces of all samples using a Hitachi TM-1000, which has the advantage of requiring no sample coating or preparation before imaging, meaning large numbers of samples can be analysed relatively quickly (higher resolution images of sample interiors are published in Yeo et al (2018) and Josso et al. (2019)). Images of surface texture were exported for every sample at both 250× and 800× magnification allowing classification of the extent of surface erosion. From over 350 samples collected during JC142, 97 were selected for this study to represent all the different regions of the seamount, all samples were identified as either FeMn pavements or FeMn lobate pavements.

2.4. Current modelling

During expedition JC142, three moorings were deployed (Fig. 1) and 36 CTD (Seabird 9plus) casts occupied across the seamount in order to investigate the hydrodynamics in the area. The moorings comprised an array of instrumentation to measure current velocities using Nortek Aquadrop DW Current Meters - on moorings A and C - and an additional TRDI Workhorse Sentinel ADCP working at 300 kHz - on mooring B - and salinity and temperature using Seabird SBE37 CTDs moored at two separate heights above the seabed (at 1000 and 2000 m above seafloor on mooring A, 9 and 900 m above seafloor on mooring B and 1000 and 3500 m on mooring C). The moorings were deployed for between 30 and 31 days. The mooring data alongside the CTD casts and real-time wind and tide data were used to generate a high-resolution hydrodynamic model of the area. Modelling was undertaken using a 500 × 500 km TELEMAC flow model around the seamount site and surrounding area, in conjunction with the Mercator Ocean global flow model at the TELEMAC model boundaries. The model computed a horizontal resolution of between 100 m and 800 m over the seamount at 49 layers through the water column (resolution is best close to the seabed and sea surface and near the centre of the seamount). For comparison with the mapping and SEM data, we used the current magnitude ($\sqrt{(U^2 + V^2)}$, where V is horizontal velocity and U is the vertical component) for a layer 1 m above the seabed. Current magnitude was extracted from this layer at all our sample locations, with one current velocity sample per hour for a week long run of the model. Maximum current vectors were also extracted at all sample locations for comparison with the slope aspect.

2.5. Mapping

Mapping was carried out using the higher-resolution bathymetry and the 400 kHz sidescan sonar mosaic collected using the AUV, as it was impossible to infer FeMn lithology from the 50 m resolution EM120 data. The detailed mapping is therefore limited to the summit of the seamount, although an overview of the lithologies observed on the slopes from the ROV footage is included in the results section. During expedition JC142 the ROV Isis had been used to collect samples and video observations of the seafloor. The samples and video footage were

used to provide the initial ground-truthing of the geophysical data. Mapping was carried out in Global Mapper v. 16, with final maps produced using QGIS 3.0 (QGIS Development Team, 2018). Changes in lithology across distances smaller than 10 m, observed from the ROV footage, were not marked so as to keep mapped units at a realistic resolution for the data. In a few rare cases, where the lithology was observed to change at this frequency, the whole area was mapped as the dominant observed lithology.

3. Results

3.1. Sample imaging and classification

Both dense, laminated pillar structures and layers of lower density, chaotic cuspate growth were observed in hand specimen cut samples and in later SEM imaging of cross sections (Yeo et al., 2018). These growth textures are separated by both erosional contacts or gradational boundaries. Erosional surfaces were regularly seen to cross cut older botryoidal growth, resulting in a complicated stratigraphy with a number of time hiatuses, representing periods of erosion (Josso et al., 2019).

Images recorded by the SEM of the surfaces of 80 FeMn crust samples distributed around the seamount revealed a variety of textures, ranging from pristine botryoidal growth textures to areas that had been completely planed flat by erosion, where the flat surface cross cuts older growth structures. These images were used to classify the crustal surfaces as: a) completely eroded, where all botryoidal growth texture had been removed leaving a smooth, flat, planar surface, b) partially eroded, where the botryoidal growth structure has been affected by erosion but the surface remains irregular, or c) pristine, where the botryoidal growth textures show no evidence of erosion (Fig. 2). The erosional surfaces can be seen to cut growth textures in high-resolution X-Ray computed tomography data presented in Yeo et al. (2018). All the samples examined from the summit of the seamount were found to have some degree of erosion, while those on the flanks were a mix of eroded and pristine. The bulk of pristine samples are found below 2000 m water depth and there is a rough correlation between erosion state and sample depth, with samples being progressively more eroded the shallower they are on the seamount.

3.2. Current modelling

Representative current magnitude profiles for different areas of the seamount are shown in Fig. 3. The current modelling shows a strong tidal influence in the currents over the seamount, with cycles of higher and lower current magnitude, with a period of around 6–8 h (Fig. 3). High water at the seamount occurs roughly half an hour before high water at the nearest mainland Port (Ad-Dakhla in the Western Sahara). The bulk of the seamount does not experience current magnitudes over 0.2 m/s at any point in the cycle and at the base almost all the current magnitudes are below 0.1 m/s. However, stronger currents break across the eastern spur of the seamount at mid-to-late-ebb in the cycle, particularly between 2000 m and the summit top at 950 m, where maximum current magnitudes reach almost 0.6 m/s during cycle peaks (the maximum current magnitude experienced by a sample in this study was 0.54 m/s) (Fig. 4). Peaks occur at similar times across most of the seamount, except on the eastern side of the summit, where they have a longer duration than elsewhere, with a single trough to trough cycle lasting around 12 h. Slightly higher maximum current magnitudes are observed on the summit of the seamount than around the base: 0.25 m/s over most of the summit versus < 0.15 m/s below 1500 m (Fig. 3).

3.3. Mapping

By combining the high-resolution sidescan sonar data with seafloor observation a geological map was produced of the summit of Tropic Seamount (Fig. 4). From ROV observation of the seafloor we recognise three different types of FeMn outcrop: pavements, which are composed of flat, planar, unbroken outcrops of FeMn crust; lobate pavements, which also form a continuous outcrop of FeMn crust but with an irregular surface and some gaps in the exposure, usually filled by sediment; and nodules, which are discrete, round or sub-round accretions of FeMn oxides, commonly precipitated around a core of a different material (Fig. 5). Plains of pelagic sediment, debris flow material and exposed underlying carbonate reef bedrock were also mapped. The flat-topped plateau forming the summit of the seamount is characterised by a number of terraces, likely produced by wave action during subsidence of the original subaerial volcanic edifice. Eight are shown in the geological map (Fig. 4) at depths of between 990 m and 1281 m. The carbonate bedrocks are almost entirely exposed around the edges of these plateaus in steep cliffs, normally < 5 m high.

Many of the largest exposures of pavement and the lobate pavement are found near the edges of these cliffs, often extending several hundred metres away from them. Other smaller areas of pavement form discrete islands in the middle of plains of mobile pelagic sediment, usually on very slight local highs, 2–4 m above the surrounding plateau. Sediment plains are concentrated in the central and southern sections of the seamount, with smaller sediment ponds also located in the north, east and west. Small debris flow deposits are found at the base of most of the carbonate cliffs, likely due to undercutting by currents and then collapse of unsupported material. The upper flanks of the seamount are also covered in debris, produced by gravitational collapse of oversteepened sections of the summit edge.

Given an entire mapped summit area of 94.8 km^2, pavement and lobate FeMn exposure cover 21.4% (12.6 km^2 and 7.8 km^2 respectively), nodules cover 13.6% (12.1 km^2), sediment plains cover 40.2% (38.1 km^2), debris covers 21.4% (20.3 km^2) and carbonate basement exposure is 3.2% (3.1 km^2). Overall, some form of FeMn deposit exposure is found on 35% of the entire summit area. However, this is likely to be a minimum estimate as crustal pavements were observed disappearing beneath rippled, mobile sedimentary deposits, suggesting that they may continue beneath some of the sedimented areas at relatively shallow burial depths.

The lack of complete high-resolution bathymetry or sidescan sonar imagery for the seamount's spurs and flanks means they were not mapped in their entirety. However, the geology observed on 39.2 km of ROV transects up the spurs is shown in Fig. 6. Here, there is a much higher exposure of FeMn lithologies than the summit – being observed on 63.2% of the transect length. These fall into the following types: pavements (19.5%), lobate pavements (38.7%) and nodules (5.0%). There is also a lower proportion of pelagic sediment (10.3%) and, despite the steep slopes, similar proportions of debris (17.9%) and carbonate outcrop (8.6%). Some differences are observed between the different spurs: a higher percentage of lobate pavements are observed in the west (56.4% compared to 17.0% in the south and 38.5% in the east) and more pavements are found in the south (35.4% compared to 10.1% in the west and 16.1% in the east).

Measured FeMn crustal thicknesses range from 5 to 170 mm and the summit samples have a similar average thickness to those on the flanks. The measured FeMn crustal thickness of the samples does not show a clear relationship with current magnitude or depth (Fig. 7).

3.4. SEM imaging: growth vs erosion

Erosion state (Section 3.1) was compared with the results from the hydrographic model (Section 3.2). Of all the samples, 17 were collected from slopes with aspects (facing directions) within thirty degrees of the maximum current direction. By facing away from the current direction, these samples are likely to be somewhat sheltered from erosion and are therefore removed from the analysis.

Initially, the modelled current magnitude, averaged over an entire week long period at each location, was compared with the erosional

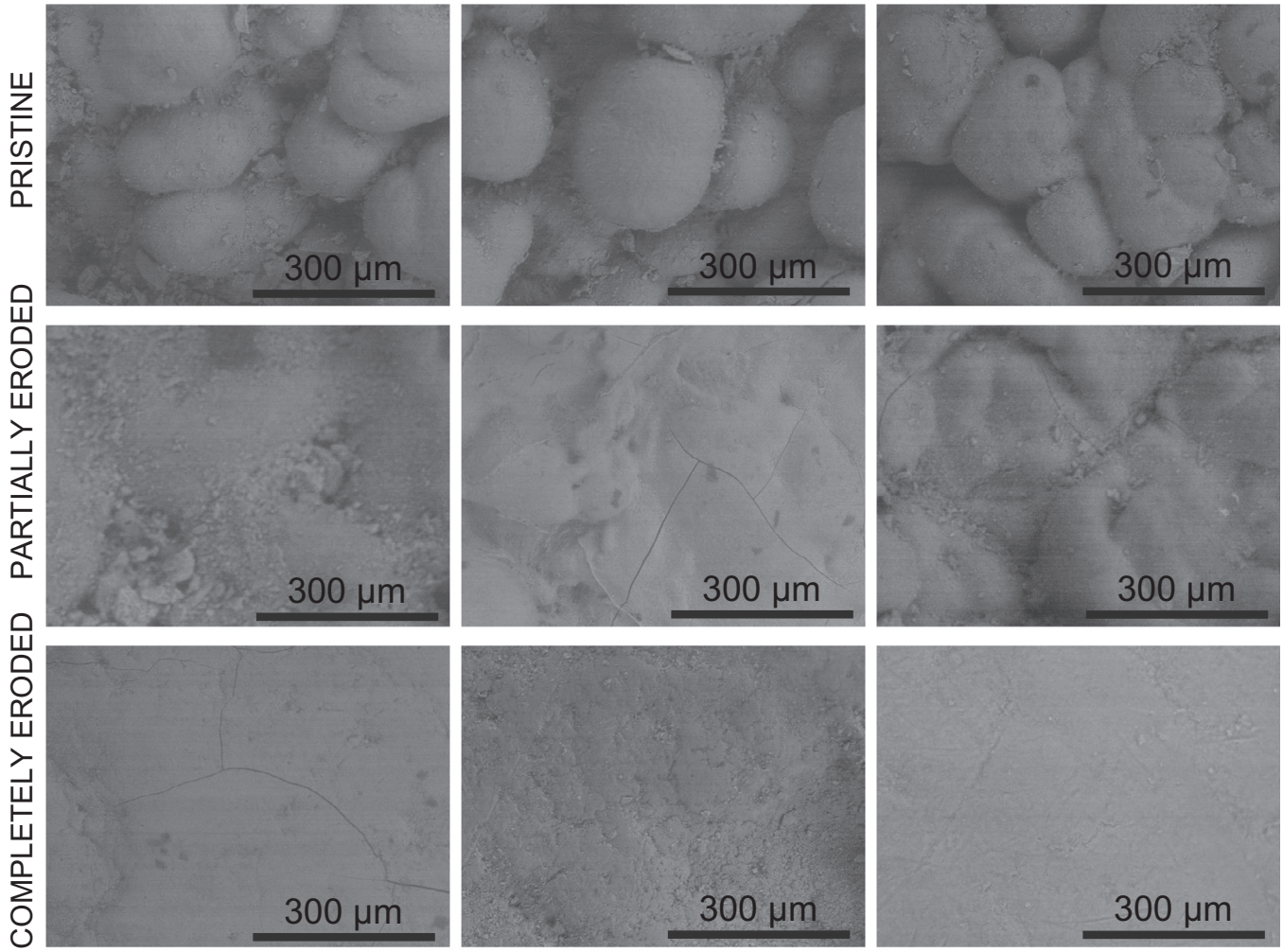

Fig. 2. SEM images showing representative surface textures and the way they are categorised. All samples with detailed botryoidal growth surfaces are classified as pristine, those totally planed flat as completely eroded and those somewhere in between as partially eroded. Images are all shown at the same scale.

state of the crusts. The pristine samples mostly experienced very low average magnitudes, with 95% of them below 0.1 m/s (Table 1). The partially and completely eroded samples experience higher average current magnitudes than the pristine samples but are very similar to each other. Therefore, the overall correlation coefficient given by:

$$Correl(X, Y) = \frac{\sum (x - \bar{x})(y - \bar{y})}{\sqrt{\sum (x - \bar{x})^2 \sum (y - \bar{y})^2}}$$

between average current magnitude and sample erosion state is 0.26 (where X and Y are different arrays, x and y represent values within these arrays and $\bar{x}$ and $\bar{y}$ represent the array means).

Given that enhanced erosion is likely to be related to periods of higher than average current magnitude, it is probably more representative to compare erosion state with the maximum and third quartile current magnitudes experienced at sample locations (Table 1). The pristine samples experience lower average maximum current magnitudes (averaging 0.17 m/s) and lower average third quartile magnitudes (averaging 0.11 m/s) than the partially and completely eroded samples which experience averaged maximum current magnitudes of up to 0.24 m/s (as high as almost 0.6 m/s for some samples (Fig. 8)) and averaged third quartile magnitudes of 0.17 m/s. There is very little difference between the maximum or third quartile current magnitudes experienced by samples classified as partially or completely eroded (Table 1), leading to low correlation coefficients of 0.21 and 0.26 respectively. There is a large spread in the magnitudes observed in each category (see Fig. 8), however, the majority of eroded samples found in low maximum current magnitude areas (< 0.2 m/s) are located on the summit (Fig. 8). The pristine samples also have average FeMn crustal thicknesses slightly greater than the partially and completely eroded samples, with average thicknesses of 46 mm compared to 41 and 37 mm for the eroded samples, although again, thicknesses are highly variable.

The outcrop patterns (Fig. 4) do not clearly correlate with current magnitude, although the mapped summit area does not include the upper slopes of the eastern spur, where the highest current magnitudes are observed. On the summit, the higher magnitude currents (> 0.2 m/s) are primarily distributed on the eastern and western sides and across the centre of the summit, with lower current magnitudes measured in the north and south (Fig. 7). However, the largest sand plains are found in the centre and in the south of the summit, covering areas of both higher and lower current magnitude. Likewise, the most expansive FeMn pavement exposures are found on the northeast and west of the seamount, again covering the spectrum of current magnitudes experienced on the summit. The ROV logs of the spurs (Fig. 6) show the high current speeds on the eastern flank correlate with an area of FeMn lobate pavement, although similar outcrops are found on the other spurs, which are experiencing lower maximum current speeds.

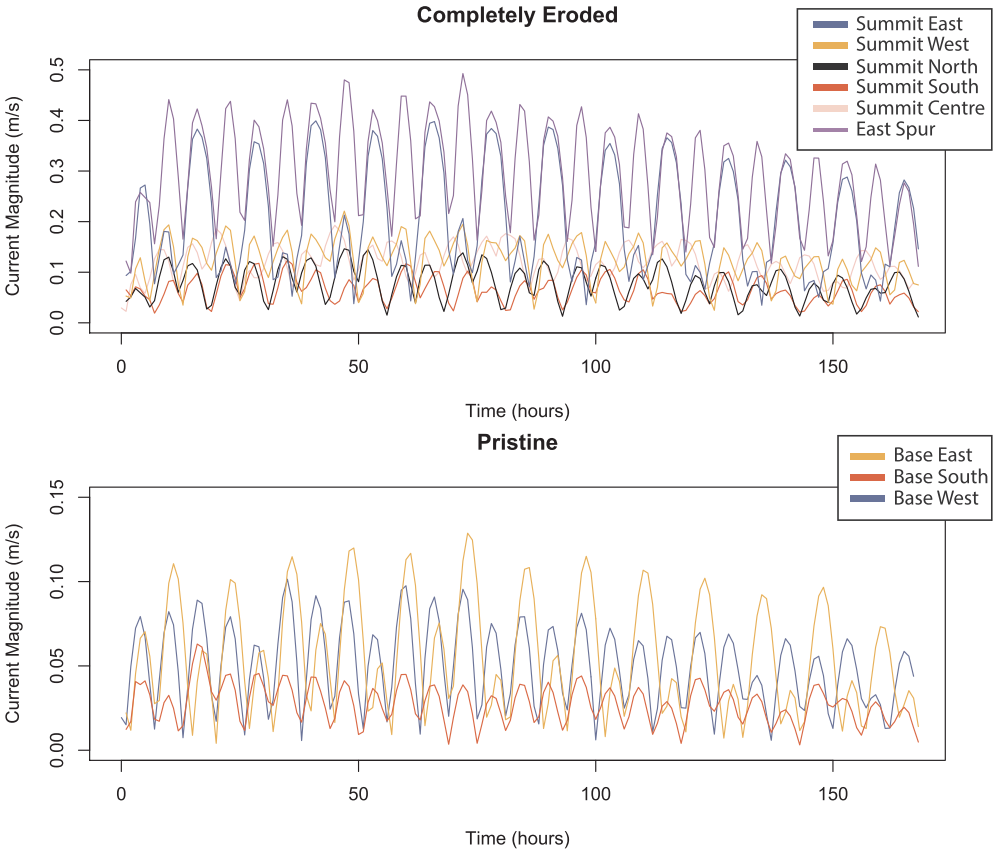

Fig. 3. Representative current magnitude profiles extracted for a week-long period at sampling locations around the seamount. The upper graph shows profiles only for samples classed as heavily eroded, and the lower graph for samples in pristine condition.

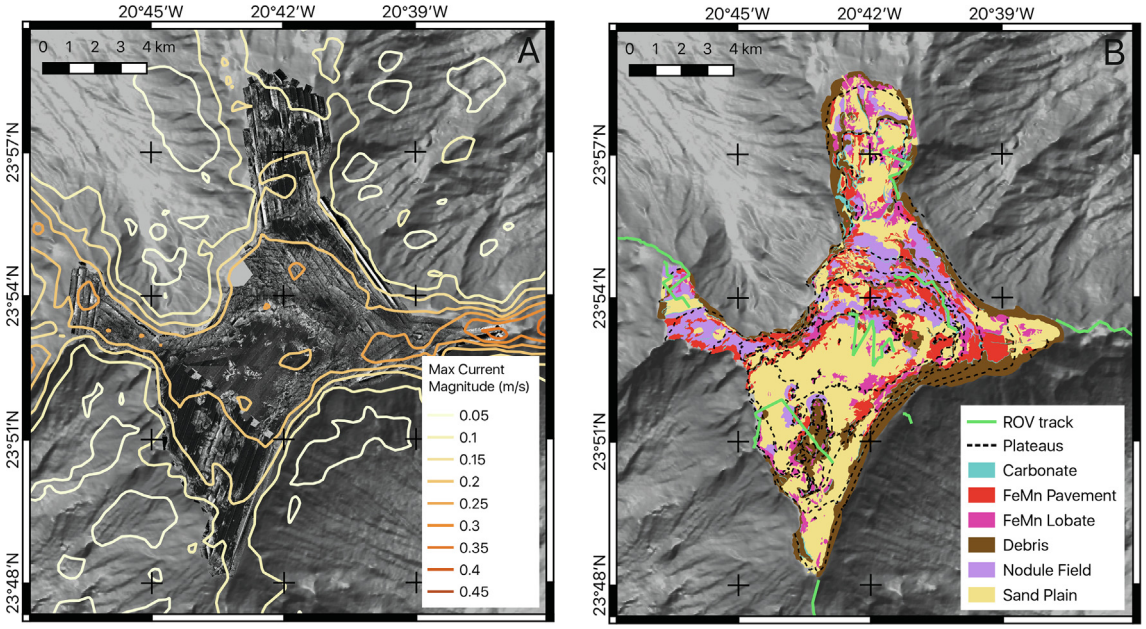

Fig. 4. (A) Sidescan sonar data of the summit collected by AutoSub6000, mosaicked at 2 m, overlaid on the EM120 bathymetry of Tropic seamount gridded at 100 m. Maximum current magnitudes are shown by the contours. (B) Geological map of the surface outcrop at Tropic Seamount. Grey dashed lines show the locations of summit plateaus, probably formed by wave action during subsidence. Green lines show the locations of ROV dives where the lithology has been ground truthed. Both maps are at the same scale for comparison. (For interpretation of the references to colour in this figure legend, the reader is referred to the web version of this article.)

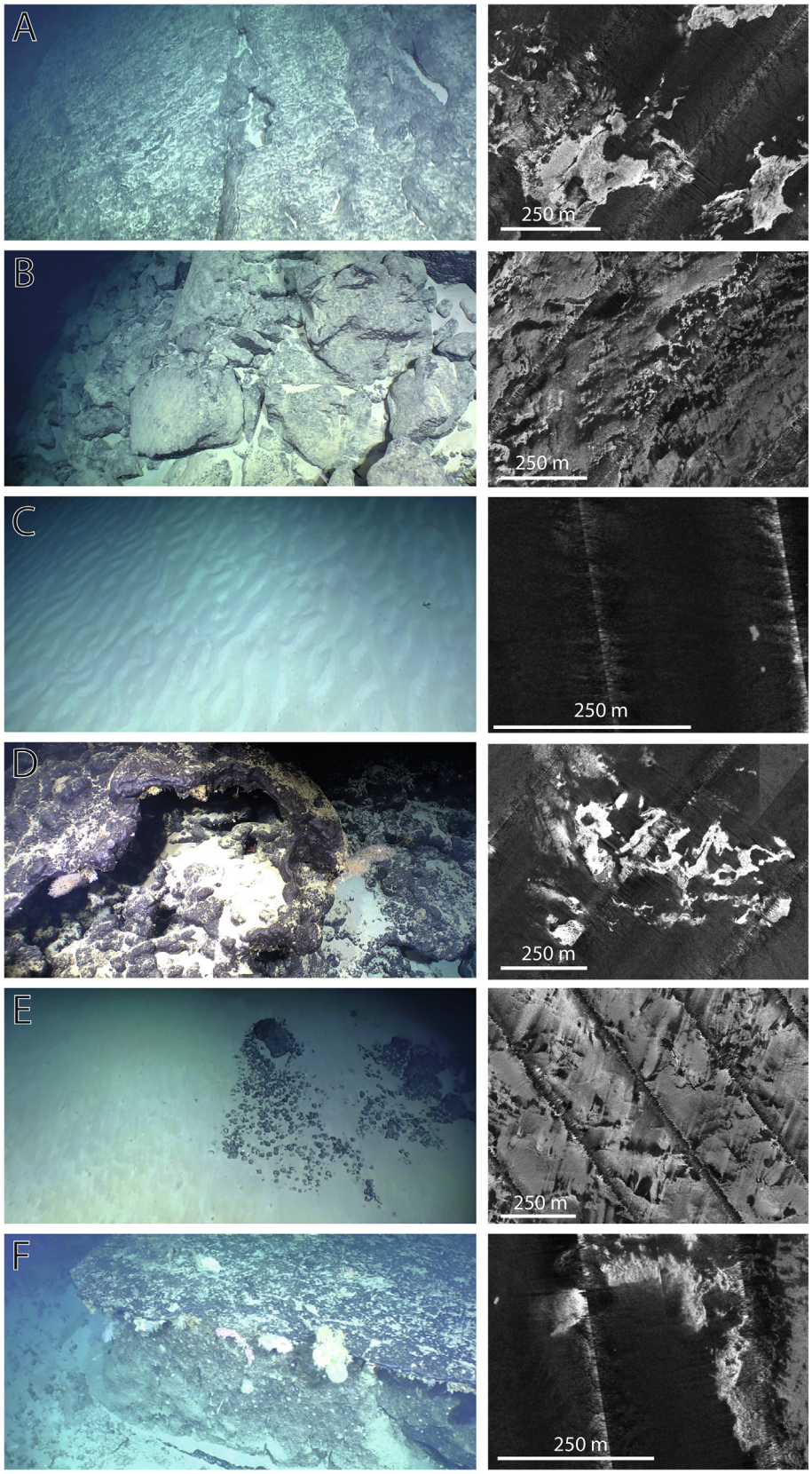

Fig. 5. Example mapped lithologies observed from the ROV footage: (A) FeMn pavement, (B) Debris, (C) Sediment Plain, (D) Lobate pavements, (E) Nodules, (F) Edge of a slightly undercut carbonate platform, with a thin FeMn crust pavement overhanging it, and the corresponding Edgetech 4200 sidescan sonar imagery collected by the AUV. Bright colours represent high reflectivity and therefore hard and/or rough surfaces. Image fields of view are approximately 3 m.

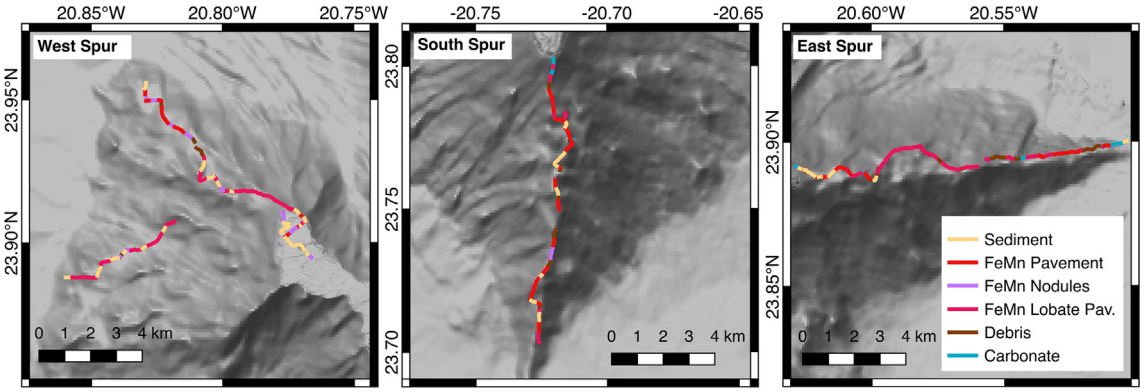

Fig. 6. Surface lithology logged from ROV video up three spurs of Tropic Seamount. No observations were made on the northern spur. Observations are overlaid on the EM120 bathymetry gridded at 100 m. All maps are shown at the same scale.

4. Discussion

4.1. FeMn outcrop distribution

The distribution of FeMn crustal outcrops, and the occurrence of nodules, does not appear to correlate clearly with high or low current magnitudes. On the summit, the pavement outcrop instead seems to be controlled by the local topography. The largest exposures of FeMn crust are found on the northern summit (Fig. 4) and on flanks that have not experienced recent gravitational collapse (i.e. those where flank collapse occurred long enough ago that FeMn deposits have had time to precipitate since) (Fig. 5). There is no simple correlation between outcrop location and modelled current magnitude (Fig. 4), however, the crustal pavement outcrops seem to be located primarily on the slopes of the flanks and near the edges of terraces which face into the strongest modelled currents. These currents will winnow loose sediments away from the terrace edges exposing harder material. These same currents are undercutting the FeMn crust pavements, eroding away the weaker carbonate basement and destabilising the overlying crust. The unsupported crust eventually collapses under its own weight forming talus at the base of the terraces. The largest nodule fields appear to be associated with these talus piles suggesting some of this material is transported down across gently sloping sediment plains at the base of the scarp while continuing to accrete FeMn oxides to form nodules. Nodules commonly accrete around fragments of hard material (e.g. Bonatti and Nayudu (1965); Hein and Koschinsky (2014); Hein et al.

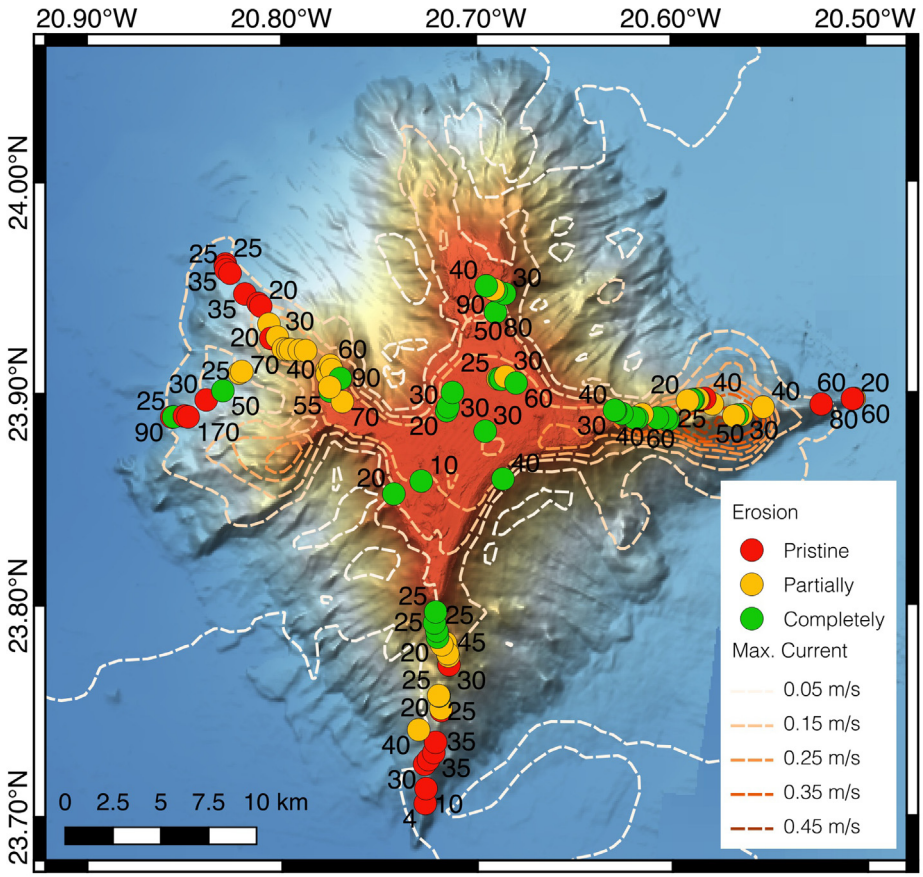

Fig. 7. Sample locations coloured according to erosion state defined from SEM images of surface textures. Contours are the maximum current magnitude extracted from the hydrographic model. All data is overlaid on the EM120 bathymetry gridded at 100 m. Black numbers are measured FeMn crustal thicknesses in mm.

Table 1
Current magnitude and crust thickness averaged across all samples in each erosion state category. Note the 2 standard deviation (2SD) for the thickness measurement is very large as a result of the large spread of thicknesses across the seamount.

	Current Magnitude (m/s)			Thickness [2SD] (mm)
	Average	Third Quartile	Maximum	
Pristine (n = 20)	0.08	0.11	0.17	45.6 [73.3]
Partially Eroded (n = 30)	0.14	0.17	0.26	40.6 [40.7]
Completely Eroded (n = 30)	0.13	0.17	0.24	36.7 [38.8]

(2012)) and talus fields would provide a large number of suitable hard fragments. Other, smaller, nodule fields have formed by hydrogenetic/diagenetic precipitation in the middle of sediment plains. On the seamount flanks, the crust seems to be kept relatively clear of pelagic sediment simply by the steep gradient. The majority of the spurs have slope gradients of between 20 and 45°, which appears to be enough to stop any major accumulation of sediment on the surfaces of the pavements.

Crustal thicknesses measured from samples are highly variable, ranging from < 1 cm to 17 cm, and are distributed around the seamount. There is no clear relationship between crustal thickness and depth, as would be expected if the crustal thickness was purely a result of the period of time available for growth. This variability in crustal thickness must, therefore, be due to a different controlling factors – either local variabilities in growth rate or modification of crusts post growth by external factors.

Josso et al. (2019) identify variability in crustal growth rates at Tropic Seamount from 1 to 24 mm/Ma during different time periods, but data are only presented for a single sample, meaning the variability in growth rate across a seamount is hard to quantify. Growth rate may be controlled by the availability of Fe and Mn colloids in the water column and variations in water chemistry surrounding the seamount (Hein et al., 2000; Koschinsky and Halbach, 1995). However, such variability would need to be occurring on very small spatial scales, which is not seen in the ocean profile (Jenkins et al., 2015). The slow-moving (10–30 cm/s) north-westerly Canary Current crosses over Tropic Seamount and supplies the area with cool, upwelled, nutrient-rich waters that stimulate primary productivity (Wooster et al., 1976; Mittelstaedt, 1991; Pelegrí and Peña-Izquierdo, 2015) but, while historic variability in the strength and nature of these currents is documented (e.g. Sarnthein et al., 1982), water chemistry would be unlikely to change substantially on the small spatial scales that characterise the thickness variations (< 100 m). Thus we conclude that oceanographic variations on a large scale are unlikely to account for the variations observed at Tropic.

It is traditionally thought that FeMn crusts form in the presence of relatively high current speeds, which will keep hard substrates swept free of sediment allowing Fe and Mn oxides to precipitate (Hein et al., 2000; Hein and Koschinsky, 2014). However, sediment bearing currents of moderate to high speeds also have the ability to mechanically erode FeMn crusts (Hein et al., 2000). Currents with near-bottom velocities of 0.3 m/s have been observed to carry sediments and erode FeMn crusts in the Central Pacific (Hein et al., 1992). Thus, it seems that FeMn crustal growth requires a fine balance of current speeds, that are high enough to sweep away pelagic sediment accumulation, but not so strong that they erode the delicate botryoidal growth surfaces of the FeMn crusts. Multiple erosional surfaces are detected for *in-situ* Tropic Seamount samples (Yeo et al., 2018, Josso et al., 2019) suggesting that erosive conditions at the same location change through time. Josso et al. (2019) recognise at least 6 hiatuses in FeMn crust growth, representing erosion or periods of non-growth during the 77 Ma of history recorded by the samples, in which around 38 My is unaccounted for suggesting that substantial proportion of crustal thickness can be removed by erosion. This erosion can also be highly localised, with erosional horizons difficult to trace between samples located just a few hundred metres from one another (Josso et al., 2019).

Yeo et al. (2018) demonstrate the crusts from Tropic Seamount are texturally very diverse, with horizons of pillared (typically < 10% detrital material) and cuspate (up to 50% bioclast/detrital material) textures, and Josso et al. (2019) identify higher growth rates in regions with higher sediment contents. However, a combination of both cuspate and pillar textures are observed in all the samples examined, with horizons difficult to cross correlate even on small spatial scales, suggesting small scale local variability in FeMn growth rate and texture may exist across the seamount. This may account for the high variability in measured crustal thickness observed all around the seamount, and may in some case obscure or complicate relationships with other external factors like erosion. It therefore seems the most likely explanation for the variable crustal thicknesses is localised erosion of material by currents and hiatuses of growth, possibly alongside locally variable growth rates.

4.2. Relationship between erosion state and current models

The distribution of erosion states across the seamount is not simple. While there appears to be a general relationship with depth – with the majority of pristine samples found below 2000 m – completely eroded samples are also found in deep water, in some places within a few hundreds of metres of the pristine samples. The presence of both eroded and un-eroded samples demonstrates that in some places the current regime is conducive to crustal growth and in other areas the current is eroding the crusts. Given that the pristine samples are all experiencing maximum current magnitudes of < 0.3 m/s and third quartile magnitudes of < 0.2 m/s, this suggests that optimal growth conditions for FeMn crusts must exist at these conditions. However, both the partially and completely eroded samples have ranges of maximum and third quartile current magnitudes that overlap with the pristine samples,

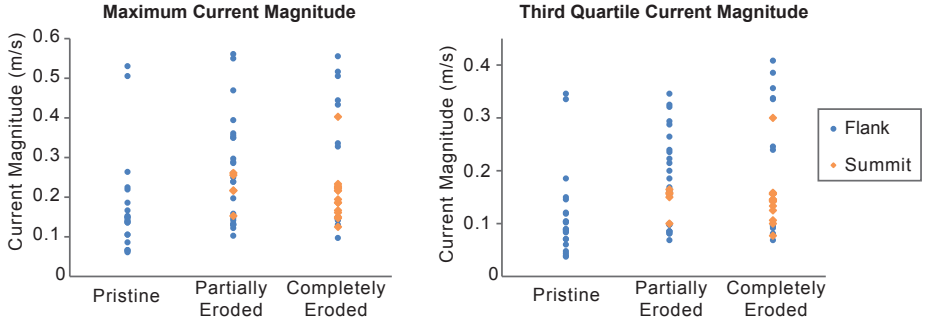

Fig. 8. Maximum and third quartile current magnitude at each sample site plotted against erosion state. Sample location (summit vs. flank) shown by marker colour.

suggesting that erosion of FeMn crusts can occur in current regimes which typically experience currents below this cut-off.

This difference in erosion state between samples above and below 0.2–0.3 m/s current magnitude is likely to be due to enhanced erosion by the mobilisation of sediments. Sediments moving along the seafloor or in the near-bottom water layer with a higher suspended sediment content will have a greater erosive effect than seawater with a low suspended sediment content (e.g. Sklar and Dietrich (2001)). Sediments collected from the summit of Tropic Seamount have D50 ≈ 200 μm and comparison of the computed peak shear stress and the threshold for mobilisation for the sediment (based on the Shield's criterion, Soulsby, 1997) suggest mobilization at current speeds of 0.26 m/s. This effect is likely to be most prevalent on the seamount summit, where we find large areas of thin, patchy sediment cover on the pavement outcrops and thicker sedimentary deposits between blocks (Fig. 5, D and F). The rippled patterns observed on sediment plain surfaces on the summit of the seamount (e.g. Fig. 5C) are further evidence of sediment mobility. This sediment enhanced erosion may explain the prevalence of completely eroded samples on the summit, compared to those on the flanks, which have lower sediment cover and tend to be partially rather that completely eroded (Fig. 7).

The existence of eroded samples at current magnitudes < 0.2 m/s is harder to explain. Based on the Shields criterion (Soulsby, 1997), erosive transport of sediments below 0.2 m/s is unlikely. Thus, the overlap between the current magnitudes experienced by pristine and eroded samples cannot be explained by this process. It is possible that higher current magnitudes and associated erosion could have occurred in the past at the sites now experiencing low current magnitudes. However, this change in currents would need to have occurred relatively recently, otherwise new growth of ferromanganese crust should be occurring on the eroded surface, and there is no evidence for major current shifts in this region in the last million years. Instead, it seems more likely that this overlap is due to the model not accurately representing the fine scale (< 100 m) detail of the currents operating around the seamount. All but one of the samples in this overlapping group lie within 50 m of a cliff or plateau edge. These features are likely to increase local current speed and turbulence, potentially above the 0.2–0.3 m/s required to erode FeMn crust and mobilize sediment. This turbulent effect is not accounted for in the current model, which predicts smooth variations in current speed, and therefore may account for the overlap observed in Fig. 8. Furthermore, the current speeds predicted by the model are not the maximum speeds the seamount will experience. Events such as storms and gyres will give rise to larger currents, which, while rare, may occur regularly enough on the million-year growth timescales required by FeMn crust to have an erosive effect, beyond that implied by the hydrodynamic model

Given the complexity of the relationship between crustal growth and currents, caution should be exercised using current models such as ours, that represent only a very short time span compared to the growth rates of the FeMn crusts, to predict FeMn crustal thicknesses and occurrence, which represents an integration of conditions over tens of millions of years. Overall crustal thickness is a combined result of variable growth rates, determined primarily by detrital/bioclast input, and current and sediment load controlled erosion. The crustal growth record at Tropic shows extremely variable growth rates of 1–24 mm/Myr cross cut by multiple erosive hiatuses (Josso et al., 2019), while the geological mapping of crust thickness shows them to be highly variable on relatively small spatial scales (regularly more than 60 mm difference within 1 km). While we do observe a slight increase in FeMn crustal thickness in regions of lower modelled currents, this degree of variability cannot be predicted using available models and therefore detailed mapping, combining high-resolution geophysical data and visual ground truthing and sampling is essential to produce realistic resource estimates for possible future exploration targets.

5. Conclusions

Ferromanganese crusts are found on both the summit and flanks of Tropic Seamount and display an array of lithologies that can be accurately mapped using a combination of high-resolution geophysical and visual survey data. At Tropic, pavement and lobate FeMn exposure cover 21.4% and nodules are found on 13.6% of the summit, meaning at least 35% of the summit has some kind of FeMn exposure, and these exposures may extend beneath some of the summit sediment packages that cover a further 40%. Exposure is better on the flanks of the seamount due to the low sediment cover.

We observe a complicated relationship between the currents predicted by the hydrodynamic model, and the locations and erosion states of the crusts. For FeMn crusts to grow, they must exist in a current regime that is both energetic enough to remove sediments from hard substrates but not so energetic that it erodes the delicate botryoidal surface growth textures. Although pristine samples are generally found at lower current magnitudes than eroded ones, some of the eroded samples also fall in areas with low current magnitudes near cliffs or plateaus. Erosion in these regions is most likely due to localised current increases and turbulence generated by these features. Overall, optimum conditions for FeMn crustal growth seem to exist at average current magnitudes < 0.1 m/s with maximum magnitudes < 0.3 m/s.

While modelling is useful to better understand the depositional conditions for ferromanganese crusts, the high degree of both temporal and spatial variability in growth rates and erosive events means that high-resolution mapping and detailed sampling is essential to fully understand the distribution of ferromanganese crust and produce realistic resource estimates.

Acknowledgements

We thank the officers and crew of Expedition 142 on board the RRS James Cook for their professionalism and commitment to achieving the scientific objectives. We thank the ROV Isis and Autosub6000 engineers for their dedication to the data acquisition. This research was funded by a Natural Environmental Research Council (NERC) grant number NE/MO11151/1. We thank Pierre Josso of the British Geological Survey for his comments on the manuscript. We are grateful to the editor and for comments from two anonymous reviewers, both of whom provided insights that greatly improved the manuscript.

References

Banakar, V.K., Hein, J.R., 2000. Growth response of a deep-water ferromanganese crust to evolution of the Neogene Indian Ocean. Mar. Geol. 162, 529–540. https://doi.org/10.1016/S0025-3227(99)00077-8.

Blum, N., Halbach, P., Münch, U., 1996. Geochemistry and mineralogy of alkali basalts from Tropic Seamount. Central Atlantic Ocean: Mar. Geol. 136, 1–19. https://doi.org/10.1016/S0025-3227(96)00057-6.

Bonatti, E., Nayudu, Y.R., 1965. The origin of manganese nodules on the ocean floor. Am. J. Sci. 263, 17–39. https://doi.org/10.2475/ajs.263.1.17.

Caress, D.W., 1999, MB-System - Public domain software for processing swath mapping sonar data: Undersea Explorations.

Clark, A., Johnson, C., Chinn, P., 1984. Assessment of Cobalt-Rich Manganese Crusts in the Hawaiian, Johnston and Palmyra Islands' Exclusive Economic Zones. Nat. Resour. Forum 8. https://doi.org/10.1111/j.1477-8947.1984.tb00484.x.

European Commission, 2017. Study on the review of the list of critical raw materials. Criticality Assessments. https://doi.org/10.2873/876644.

Halbach, P.E., Jahn, A., Cherkashov, G., 2017. Marine co-rich ferromanganese crust deposits: description and formation, occurrences and distribution, estimated world-wide resources. In: Sharma, R. (Ed.), Deep-Sea Mining: Resource Potential, Technical and Environmental Considerations. Springer, Cham, pp. 1–535. https://doi.org/10.1007/978-3-319-52557-0.

Halbach, P., Puteanus, D., 1984. The influence of the carbonate dissolution rate on the growth and composition of Co-rich ferromanganese crusts from Central Pacific seamount areas. Earth Planet. Sci. Lett. 68, 73–87. https://doi.org/10.1016/0012-821X(84)90141-9.

Hein, J.R., Koschinsky, A., 2014. Deep-ocean ferromanganese crusts and nodules. In: Treatise on Geochemistry. Elsevier, pp. 273–291. https://doi.org/10.1016/B978-0-08-095975-7.01111-6.

Hein, J.R., Bohrson, W.A., Schulz, M.S., Noble, M., Clague, D.A., 1992. Variations in the

fine-scale composition of a central pacific ferromanganese crust: paleoceanographic implications. Paleoceanography 7, 63–77. https://doi.org/10.1029/91PA02936.
Hein, J.R., Koschinsky, A., Bau, M., Manheim, F.T., Kang, J., Roberts, L., 2000. Cobalt-rich ferromanganese crusts in the pacific. In: Cronan, D.S. (Ed.), Handbook of Marine Mineral Deposits. New York, CRC Press, Boca Raton, pp. 239–279.
Hein, J.R., Conrad, T.A., Dunham, R.E., 2009. Seamount characteristics and mine-site model applied to exploration- and mining-lease-block selection for cobalt-rich ferromanganese crusts. Mar. Georesour. Geotechnol. 27, 160–176. https://doi.org/10.1080/10641190902852485.
Hein, J.R., Conrad, T.A., Staudigel, H., 2010. Seamount Mineral Deposits: a source of rare metals for high-technology industries. Oceanography v. 23, 184–189. https://doi.org/10.5670/oceanog.2010.70.
Hein, J.R., Conrad, T.A., Frank, M., Christl, M., Sager, W.W., 2012. Copper-nickel-rich, amalgamated ferromanganese crust-nodule deposits from Shatsky Rise. NW Pacific: Geochem., Geophys., Geosyst. 13, 1–23. https://doi.org/10.1029/2012GC004286.
Hein, J.R., Mizell, K., Koschinsky, A., Conrad, T.A., 2013. Deep-ocean mineral deposits as a source of critical metals for high- and green-technology applications: comparison with land-based resources. Ore Geol. Rev. 51, 1–14. https://doi.org/10.1016/j.oregeorev.2012.12.001.
Ingram, B.L., Hein, J.R., Farmer, G.L., 1990. Age determinations and growth rates of Pacific ferromanganese deposits using strontium isotopes. Geochim. Cosmochim. Acta 54, 1709–1721. https://doi.org/10.1016/0016-7037(90)90402-7.
Jenkins, W.J., Smethie, W.M., Boyle, E.A., Cutter, G.A., 2015. Water mass analysis for the U.S. GEOTRACES (GA03) North Atlantic sections. Deep Sea Res. Part II 116, 6–20. https://doi.org/10.1016/j.dsr2.2014.11.018.
Josso, P., Parkinson, I., Horstwood, M., Lusty, P., Chenery, S., Murton, B., 2019. Improving confidence in ferromanganese crust age models: a composite geochemical approach. Chem. Geol. 513, 108–119. https://doi.org/10.1016/j.chemgeo.2019.03.003.
Klemm, V., Levasseur, S., Frank, M., Hein, J.R., Halliday, A.N., 2005. Osmium isotope stratigraphy of a marine ferromanganese crust. Earth Planet. Sci. Lett. 238, 42–48. https://doi.org/10.1016/j.epsl.2005.07.016.
Koschinsky, A., Halbach, P., 1995. Sequential leaching of marine ferromanganese precipitates: genetic implications. Geochim. Cosmochim. Acta 59, 5113–5132. https://doi.org/10.1016/0016-7037(95)00358-4.
Koschinsky, A., van Gerven, M., Halbach, P., 1995a. First investigations of massive ferromanganese crusts in the N.E Atlantic in comparison to hydrogenetic Pacific occurrences. Mar. Georesour. Geotechnol. 13, 375–391. https://doi.org/10.1080/10641199509388294.
Koschinsky, A., Van Gerven, M., Halbach, P., 1995b. First investigations of massive ferromanganese crusts in the NE Atlantic in comparison with hydrogenetic pacific occurrences. Mar. Georesour. Geotechnol. 13, 375–391. https://doi.org/10.1080/10641199509388294.
Koschinsky, A., Halbach, P., Hein, J.R., Mangini, A., 1996. Ferromanganese crusts as indicators for paleoceanographic events in the NE Atlantic. Geologische Rundschau 85, 567–576. https://doi.org/10.1007/BF02369011.
Koschinsky, A., Hein, J.R., 2003. Uptake of elements from seawater by ferromanganese crusts: solid-phase associations and seawater speciation. Mar. Geol. 198, 331–351. https://doi.org/10.1016/S0025-3227(03)00122-1.
Krishnaswami, S., Kirk Cochran, J., 1978. Uranium and thorium series nuclides in oriented ferromanganese nodules: growth rates, turnover times and nuclide behavior. Earth Planet. Sci. Lett. 40, 45–62. https://doi.org/10.1016/0012-821X(78)90073-0.
Lusty, P.A.J., Hein, J.R., Josso, P., 2018. Formation and occurrence of ferromanganese crusts: earth's storehouse for critical metals. Elements 14, 313–318. https://doi.org/10.2138/gselements.14.5.313.
Lusty, P.A.J., Murton, B.J., 2018. Deep-ocean mineral deposits: metal resources and windows into earth processes. Elements 14, 301–306. https://doi.org/10.2138/gselements.14.5.301.
Manheim, F.T., 1986. Marine cobalt resources. Science 232, 600–608. https://doi.org/10.1126/science.232.4750.600.
Marino, E., González, F.J., Somoza, L., Lunar, R., Ortega, L., Vázquez, J.T., Reyes, J., Bellido, E., 2017. Strategic and rare elements in Cretaceous-Cenozoic cobalt-rich ferromanganese crusts from seamounts in the Canary Island Seamount Province (northeastern tropical Atlantic). Ore Geol. Rev. 87, 41–61. https://doi.org/10.1016/j.oregeorev.2016.10.005.
Mitchell, N.C., 2001. Transition from circular to stellate forms of submarine volcanoes. J. Geophys. Res.: Solid Earth 106, 1987–2003. https://doi.org/10.1029/2000JB900263.
Mittelstaedt, E., 1991. The ocean boundary along the northwest African coast: circulation and oceanographic properties at the sea surface. Prog. Oceanogr. 26, 307–355.
Palomino, D., Vázquez, J.-T., Somoza, L., León, R., López-González, N., Medialdea, T., Fernández-Salas, L.-M., González, F.-J., Rengel, J.A., 2016. Geomorphological features in the southern Canary Island Volcanic Province: the importance of volcanic processes and massive slope instabilities associated with seamounts. Geomorphology 255, 125–139. https://doi.org/10.1016/j.geomorph.2015.12.016.
Pelegrí, J.L., Peña-Izquierdo, J., 2015. Inorganic nutrients and dissolved oxygen in the Canary Current Large Marine Ecosystem. In: Valdés, L., Déniz-González, I. (Eds.), Oceanographic and biological features in the Canary Current Large Marine Ecosystem. IOC-UNESCO, Paris, pp. 133–142 IOC Technical Series.
Petersen, S., Krätschell, A., Augustin, N., Jamieson, J., Hein, J.R., Hannington, M.D., 2016. News from the seabed – geological characteristics and resource potential of deep-sea mineral resources. Mar. Policy 70, 175–187. https://doi.org/10.1016/j.marpol.2016.03.012.
Price, J.G., 2011. Energy critical elements: securing materials for emerging technologies. Min. Eng. 43, 33–34.
QGIS Development Team, 2018, QGIS Geographic Information System.: Open Source Geospatial Foundation Project., http://qgis.osgeo.org.
Rona, P.A., 2003. Resources of the Sea floor. Science 299, 673–674. https://doi.org/10.1126/science.1080679.
Sandwell, D.T., Müller, R.D., Smith, W.H.F., Garcia, E., Francis, R., 2014. New global marine gravity model from CryoSat-2 and Jason-1 reveals buried tectonic structure. Science 346, 65–67. https://doi.org/10.1126/science.1258213.
Sarnthein, M., Thiede, J., Pflaumann, U., Erlenkeuser, H., Fütterer, D., Koopmann, B., Lange, H., Seibold, E., 1982. Atmospheric and Oceanic Circulation Patterns off Northwest Africa During the Past 25 Million Years BT – Geology of the Northwest African Continental Margin. Heidelberg, Springer, Berlin Heidelberg, pp. 545–604.
Sklar, L.S., Dietrich, W.E., 2001. Sediment and rock strength controls on river incision into bedrock. Geology 29, 1087. https://doi.org/10.1130/0091-7613(2001)029<1087:sarsco>2.0.co;2.
Soulsby, R., 1997. In: Dynamics of Marine Sands. Thomas Telford Publishing. https://doi.org/10.1680/doms.25844.
van den Bogaard, P., 2013. The origin of the Canary Island Seamount Province – new ages of old seamounts. Sci. Rep. 3, 2107. https://doi.org/10.1038/srep02107.
Vogt, P.R., Smoot, N.C., 1984. The Geisha Guyots: multibeam bathymetry and morphometric interpretation. J. Geophys. Res.: Solid Earth 89, 11085–11107. https://doi.org/10.1029/JB089iB13p11085.
Wessel, P., Sandwell, D.T., Kim, S., 2010. The global seamount census. Oceanography 23, 24–33.
Wooster, W.S., Bakum, A., McLain, D.R., 1976. The seasonal upwelling cycle along the eastern boundary of the North Atlantic. J. Mar. Res. 34, 131–140.
Yeo, I., Dobson, K., Josso, P., Pearce, R., Howarth, S., Lusty, P., Le Bas, T., Murton, B., 2018. Assessment of the mineral resource potential of atlantic ferromanganese crusts based on their growth history. Microstruct., Texture: Miner. 8. https://doi.org/10.3390/min8080327.